4

Fabrication of Bio-nanocomposite Nanofibers Mimicking the Mineralized Hard Tissues via Electrospinning Process

Gyeong-Man Kim
Fraunhofer Institute for Cell Therapy and Immunology,
Perlickstraße 1, 04103 Leipzig,
Germany

1. Introduction

From physicochemical point of view, e.g, the architecture and the chemistry, mineralized hard tissues such as bone and dentin can be considered as unique "living nanocomposites". They are nature-made materials, which common exhibit highly complex and strongly hierarchical structures on different length scales [1-3]. Microscopically, in the lowest level of such mineralized hard tissue the minerals are deposited in parallel fashion into a structured organic matrix, yielding a highly anisotropic three-dimensional structure [4]. The mineral components are calcium phosphates known as mainly hydroxyapatite (HAp) nanocrystals with formula $Ca_{10}(PO_4)_6(OH)_2$ [5,6], having a plate-like shape with highly variable length (20-40 nm), width (~20nm) and thickness (~1.5-5 nm) dimensions. While the inorganic components are predominantly responsible for the mechanical properties of hard tissues, the organic matrix not only gives them their toughness but also contains the osteoblasts, odontoblasts and mixtures of type I collagen and specialized non-collagenous proteins, including growth factors necessary for continual growth and repair [7].

In spite of high demand in clinical medicine, nature's ability to self-organize inorganic component with preferred orientation in the bioorganic matrix is still not reproducible by synthetic procedures because of their complex nature. Therefore, in fields ranging from biology and chemistry to materials science and bioengineering a big challenge is being required to facilitate fabrication of bone and dentin-like biocomposite materials, which may allow the ingrowth of hard tissues with improving the mechanical properties with respect to the hard tissue regeneration. Several major requirements, which are critical in the development of biomaterials for hard tissue regeneration purpose, have to be taken into account: (1) the material must have a positive influence on the amount and quality of newly formed hard tissue, (2) the material must shorten the period of hard tissue formation and healing process of damaged tissues, (3) the material must not cause any adverse effects, namely inflammatory or toxic response, and (4) it must obtain mechanical properties that match with the natural hard tissues [8,9].

In recent years, particular attention has been paid to the biomimetic approaches, which allow us to mimic such nature-made bio-inorganic and bio-organic composite materials [10]. The main idea in biomimetic approaches is to control and fabricate the morphology and the

Source: Nanofibers, Book edited by: Ashok Kumar,
ISBN 978-953-7619-86-2, pp. 438, February 2010, INTECH, Croatia, downloaded from SCIYO.COM

composition of developed biomaterials, in which the nanocrystallites of inorganic compounds are being dispersed with preferential orientation in the organic matrices. Owing to its large potential in biomedical applications, many studies have been reported the preparation of bone-like biocomposites of HAp and bioactive organic components such as collagen, chondroitin sulfate, chitosan and amphiphilic peptide by direct precipitation [11-13], poly(lactic acid) through a solvent-cast technique [14,15], and polyamide by solution method [16,17]. Some studies showed a similar nanostructure to bone, in which the crystallographic *c*-axes of the HAp were regularly aligned along the collagen fibers [18]. Additional studies have also demonstrated the preparation of collagen/HAp composites by anchoring of HAp particles in the collagen matrix [19,20]. Although these nanocomposites exhibited high biocompatibility and improved mechanical properties with similar chemical composition to natural bone, they did not show any complex hierarchical nanostructures as bone.

Recently, electrospinning technique has received a growing attention because polymer fibers prepared by this technique achieve fiber diameters in the range from micrometers down to a few nanometers straightforwardly and cost-effectively [21,22]. In a typical process, a polymer solution is forced through a capillary, forming a pendent drop at the tip of capillary. Then a high voltage is applied between the capillary and a grounded collection target. When the electric field strength overcomes the surface tension of the droplet, a polymer solution jet is initiated and accelerated toward the collection target. As the jet travels through the air, the solvent evaporates and a non-woven polymeric fabric is formed on the target. Because the resulting non-woven fabrics often resemble the superstructure features of natural extra cellular matrix, they have gained a great interest in tissue engineering as scaffold materials for tissue regeneration, immobilized enzymes and catalyst systems, and wound dressing articles. In addition, the high specific surface area and highly porous three-dimensional structure enables their use in high density cell and tissue cultures. To date, it has been well established that the ES process allows easy incorporation of particles with different habits, such as 1-dimensional carbon nanotubes [23,24], 2-dimensional layered silicates [25-27] or 3-dimensional SiO_2 nanoparticles [28] and many others [29], into the nanofibers.

Although pure HAp rarely occurs in biological systems, the synthetic HAp has been proven to possess excellent biocompatibility, bioactivity and osteoconduction [30,31]. These characteristics are most probably attributed to its chemical composition and crystallographic structure similar to those of the mineral part of natural biominerals occurring in bone, dentine, cartilage, tendons and ligaments [32,33]. Therefore, to date, the synthetic HAp has been used with a great attention in widespread biomedical applications such as fillings and/or substitutes for bulk bone defects or voids in the form of powders, porous blocks or granules, and coatings for orthopedic (e.g. hip-joint prosthesis) and dental implants [34-36].

Based on the above mentioned considerations, in the present work we successfully mimicked bio-nanocomposite fibers to the lowest level of hierarchical organization similar to bone. Our approach comprised using the electrospinning technique on the basis of PVA as matrix and HAp nanoparticles as the inorganic phase for hard tissue regeneration purpose [37]. To our best knowledge, such kind of bone-like electrospun fibers based on the biocompatible polymer with HAp has not yet been documented. The idea to use PVA is supported by several factors: PVA is one of the well-known water-soluble synthetic polymers and the backbone chains are highly interconnected by hydrogen bonding because

of the presence of abundant hydroxyl groups. These characteristics contribute to an excellent chemical resistance and mechanical properties, including high tensile and impact strength or creep resistance. On the other hand, the hydroxyl groups can be used to securely incorporate molecules of biological species, such as collagens, hyaluronan [38] or deoxyribonucleic acid [39]. PVA is truly biodegradable with nontoxic byproducts being water and carbon dioxide and it is highly biocompatible [40] with living organs and cells, which leads to broad biomedical and pharmaceutical applications [41,42]. In addition, PVA/HAp nanocomposites (NC) were chosen for two reasons: (1) PVA can strongly interact with the surface of HAp, because PVA is hydrophilic and HAp has hydroxyl groups on the surface, and thus (2) PVA/HAp NC can conveniently be electrospun from an aqueous medium.

The capability and feasibility of the technique presented in this work provides a promising alternative approach for the fabrication of bio-nanocomposite fibers. These fibers provide widespread future applications related to hard tissue (bone and dentin) replacement and coating implants, because of their resemblance to the nanostructure of living bone from the physiochemical point of view.

2. Results and discussion

2.1 Morphology and crystal structure of HAp

Figure 1a shows a TEM micrograph of HAp particles, in which the morphology of the individual HAp particles is clearly revealed to be rod-like shape. By semi-quantitative analysis, the particles had width of 10 to 30 nm (with an average of ~18 nm) and lengths of 20 to 120 nm (average of ~50 nm) (see Figure 1b) [44]. To get more detail of surface and crystal structure of HAp we performed HR-TEM. Figure 2a shows an overview image of agglomerates of HAp nanoparticles. The image indicates that HAp nanoparticles consist of well defined crystalline rods. Hence, hereafter, we denote HAp nanoparticles to HAp nanorods.

Most striking feature obtained from TEM investigation is that all HAp nanorods exhibit nanoporous morphology on the surface. Such electron-lucent nanopores were reported by several authors, suggesting that the voids were sublimation holes caused by electron beam damage [45]. However, at least, based on our results we exclude this argument, because the nanopores always appeared, even if the duration and dose of electron beam on the HAp during TEM were rigorously changed. Therefore, it could be concluded that such nanoporous morphology is an intrinsic nature of our HAp nanorods [46]. High porosity on the HAp surface may provide cell anchorage sites and structural guidance. In addition, and within an *in vivo* milieu, they provide the interfaces to respond to the physiological and biological clues and to remodel the extracellular matrix integrating with the surrounding native tissue.

In Figure 2b a HR-TEM image of a single isolated HAp nanorod along the [010] zone axis together with its corresponding fast Fourier transform (FFT) pattern is shown. A calculated inter-planar spacing between vertical dark and white lines (d-spacing) of a prevailing HR-TEM fringe is 0.342 nm, normal to the long axis of the HAp nanocrystal, i.e., the c-lattice planes corresponding to the (002) reflection. In addition, FFT pattern showed several sets of lattice fringes corresponding to spacing of 0.827 nm, 0.463 nm, 0.386 nm, 0.317 nm and 0.278 nm, which are attributed to the (100), (110), (111), (102) and (112) planes, respectively (discussed as following in XRD).

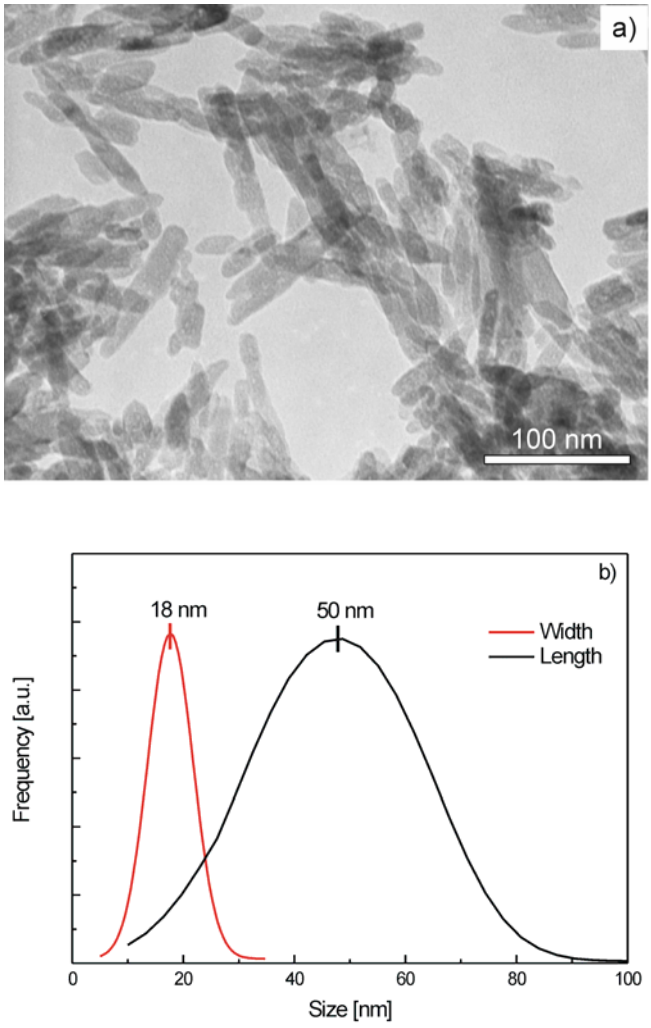

Fig. 1. a) TEM micrograph of HAp nanoparticles and b) particle size distribution.

To identify the crystal structure and lattice fringes of HAp nanorods compared with HR-TEM data we carried out the XRD measurements. The X-ray powder diffraction pattern of pure HAp nanoparticles is shown in Figure 3. The observed positions (2θ) and their corresponding $d_{2\theta}$ and indices (hkl) from the XRD pattern of HAp nanoparticles are listed in table 1. The XRD profile of the HAp is indexed with the cell dimensions a = 0.941 nm, c = 0.69 nm, and the structural refinements are carried out in the $P6_3/m$ space group [47]. No noticeable diffraction peak appears other than that of HAp. These results suggest that the *d* spacings of the corresponding planes of our HAp nanoparticles are in good agreement with those on the JCPDS card (No 9-432).

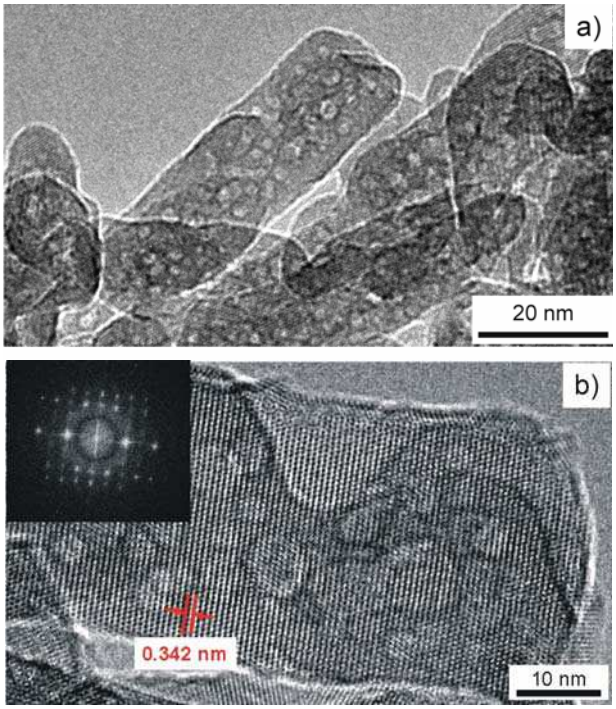

Fig. 2. a) HR-TEM overview image of agglomerates of Hap nanoparticles and b) micrograph of overview HAp nanoparticles, showing the nanoporous morphology and b) HR-TEM image of a single HAp nanorod with its corresponding FFT pattern (as inset).

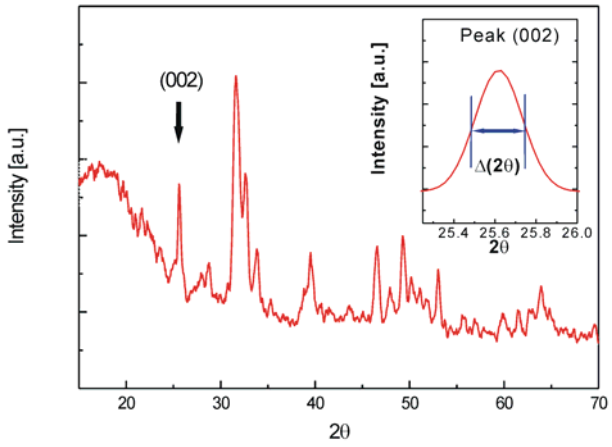

Fig. 3. XRD pattern of pure HAp nanorods. Inset indicates the enlarged (002) reflection (denoted with an arrow) used for calculation of the crystal size.

To estimate the crystal size of the HAp nanoparticles we applied the Scherrer's equation (eq. (1)) for the broadening of the corresponding X-ray spectral peaks [48]:

$$L = \frac{K\lambda}{B(2\theta)\cos\theta} \quad (1)$$

where L is the crystallite size, K is a constant taken as the default value of 0.89, λ is the wavelength of the x-ray, B(2θ) is the full width at the half maximum intensity (FWHM) and θ is the Bragg angle. The width of the diffraction peak with the intensity (002) was selected for the calculation (see inset in Figure 3). The estimated crystallite size L of Hap is 18.1 nm. This is well consistent with that from TEM measurements (average 17.7 nm).
Based on the analysis of TEM, HR-TEM and XRD, it can be concluded that the HAp nanorods are high quality crystals containing nanopores. The rods exhibit a growing direction along [001] with a d-spacing of 0.68 nm along its long axis.

2θ	$d_{2\theta}(nm)$	hkl
25.8	0.34	002
31.8	0.28	211
32.8	0.27	300
34.0	0.26	202
39.8	0.23	310
46.5	0.20	222
48.1	0.19	312
49.4	0.18	213
53.1	0.17	004

Table I. 2θ-values observed from XRD pattern of pure HAp nanorods, d-values determined from 2θ- values ($d_{2\theta}$) and corresponding indices (hkl)

2.2 Morphology and crystalline structure of ES-PVA fibers with and without HAp

Figure 4a shows a representative SEM micrograph for the electrospun fibers of pure PVA. Using water as solvent and combination of optimal electrospinning conditions (6 cm of working distance, 10 kV of operating voltage), the average diameter of ES fibers is approximately 160 nm without any sign of bead formation. The structure of electrospun fibers from PVA/HAp nanocomposite is just identical to those from pure PVA, except for minor difference in their average size. The average diameter of ES-fibers shifts from 160 nm to 170 nm upon addition of HAp (see Figure 4b). Nevertheless, the majority of diameter in both cases lies in the range of 100 to 250 nm.
In order to discern any variation in crystalline content as a result of HAp addition to the PVA the XRD measurements on the electrospun fibers PVA with and without HAp were carried out and the resulting XRD patterns were analyzed in more detail (see Figure 5). In the case of the electrospun pure PVA fibers, the diffraction peaks reveal at 2θ = 19.5° (d-spacing = 0.454 nm) and 40.5° (d-spacing = 0.223 nm) [49]. The peak corresponds to a typical doublet reflection of (101) and (10-1) planes of the semicrystalline atactic PVA, which contain the extended planar zigzag chain conformation, while the latter belongs to the (220) reflection [50]. This diffraction profile indicates that the electrospun fibers are still preserved

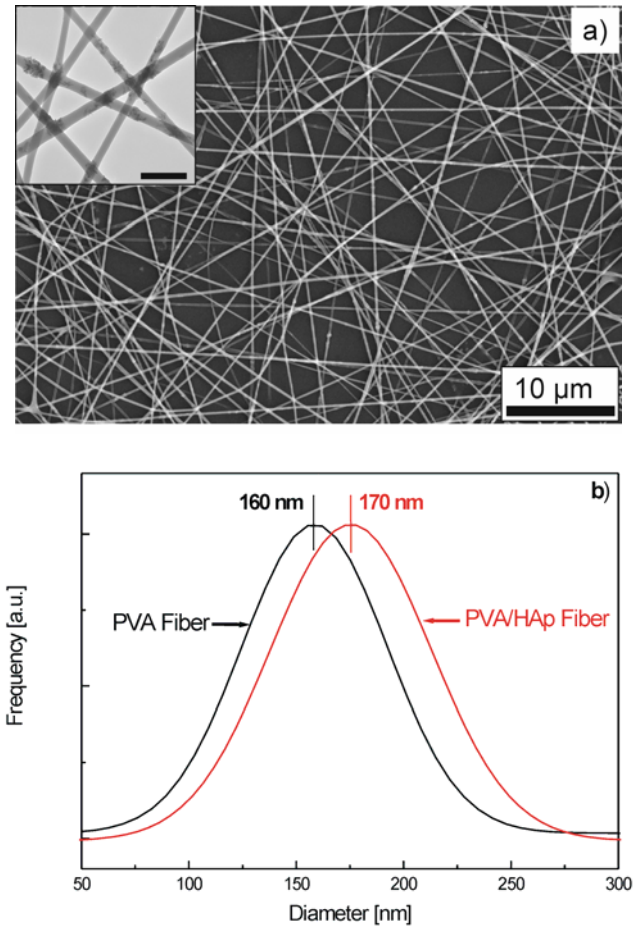

Fig. 4. a) SEM and TEM (as inset, scale bar indicates 100 nm) micrographs of as-electrospun PVA/HAp nanocomposite fibers and b) diameter distribution of ES-PVA and -PVA/HAp nanocomposite fibers.

in its semicrystalline nature associated with the trans-planar chain conformation. This could be attributed to the fact that due to the intense intermolecular hydrogen bonding the PVA chains retain their trans-planar chain conformation even under the ultra-high shear stress during the electrospinning process.

In contrast, after integrating HAp nanorods into PVA, as seen in Figure 5, the position of the doublet peak slightly is shifted to a lower value, implying an increase in the size of the PVA crystallites. In addition, the peak area is broadened to some extent, indicating that the crystallinity of PVA is suppressed by the introduction of HAp into the PVA matrix. From close inspection of the doublet peak (see inset in Figure 5) this result is clearly evidenced by an increase of d-spacing from 0.454 nm to 0.462 nm corresponding to the peak position at $2\theta = 19.5°$ and 19.2^{o} for ES-PVA and ES-PVA/HAp, respectively. The increase in the

crystalline thickness might be attributed to the high packing efficiency of the tie molecules in the amorphous regions within the electrospun fibers. As a consequence, the overall diameter of electrospun fibers increased by the introduction of HAp into PVA fiber matrix. The suppression of the crystallinity, i.e., broadening of peak area, should be attributed to the structural change from the lamellar structure to the microfibrillar structure associated with the lamellar break-up by strong elongational stress during electrospinning. Applying the Debye-Scherer Equation (1) with regard to the broadening of the doublet peak we have estimated the average crystallite size, L, corresponding to the microfibril diameter of PVA crystallite; 3.2 nm and 2.7 nm for the ES-PVA fibers and ES-PVA/HAp fibers, respectively.

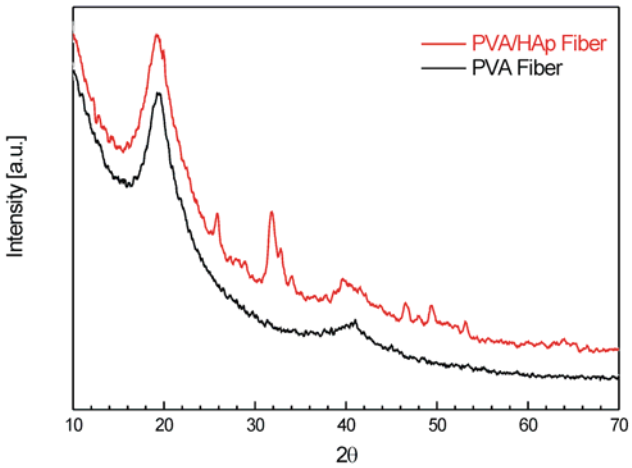

Fig. 5. XRD patterns of electrospun PVA and PVA/HAp nanocomposite fibers. The scans are shifted along the y-axis for clarity.

It should be noted that the suppression of crystallinity for the electrospun fibers compared with the bulk polymer is a general occurrence. The electrospinning process is associated with a high shear stress and a very rapid structure formation of the polymer material, thus this method gives rise to a less appropriate environment to form perfect crystallites as in the bulk. Further suppression of PVA crystallinity in the electrospun fibers upon introducing HAp is caused by destruction of the orientation order of the macromolecule chains and even by formation of amorphous bound layers around the HAp nanoparticles. The first reason means that the HAp nanorods act as steric hindrances within the electrospun fibers, and thus the crystallization is restricted by a decreasing amount of intact crystalline region. The latter could be envisaged as a fact that the strong interaction caused by hydrogen bonding leads to trap PVA molecules onto the HAp nanorods coupled with their large specific surface areas. As a consequence, the regular planar zigazag conformation collapses and converts into an amorphous structure on the interfacial region of Hap. Thus, the overall crystallinity of PVA is decreasing when the HAp nanorods are incorporated into the PVA matrix. This result is well consistent with the DSC measurements as described later.

The typical internal morphology of the electrospun fibers containing HAp is shown in Figure 6a. It is clearly seen that the HAp nanorods are well distributed within the electrospun fiber and, of most interest, a large number of HAp nanorods are preferentially oriented parallel to the longitudinal direction of the electrospun PVA fibers. A HR-TEM image of a single isolated HAp nanoparticle with the corresponding fast Fourier transform (FFT) pattern is shown in Figure 6b. It can be clearly confirmed that the d-spacing of (001) plane of HAp, i.e. the crystallographic *c*-axis, oriented normal to the long axes of the PVA fiber. As mentioned above, the ultra-high shear stress upon electrospinning not only induces an orientation of macromolecules but also properly initiates the alignment of nanorods of HAp to a large extent.

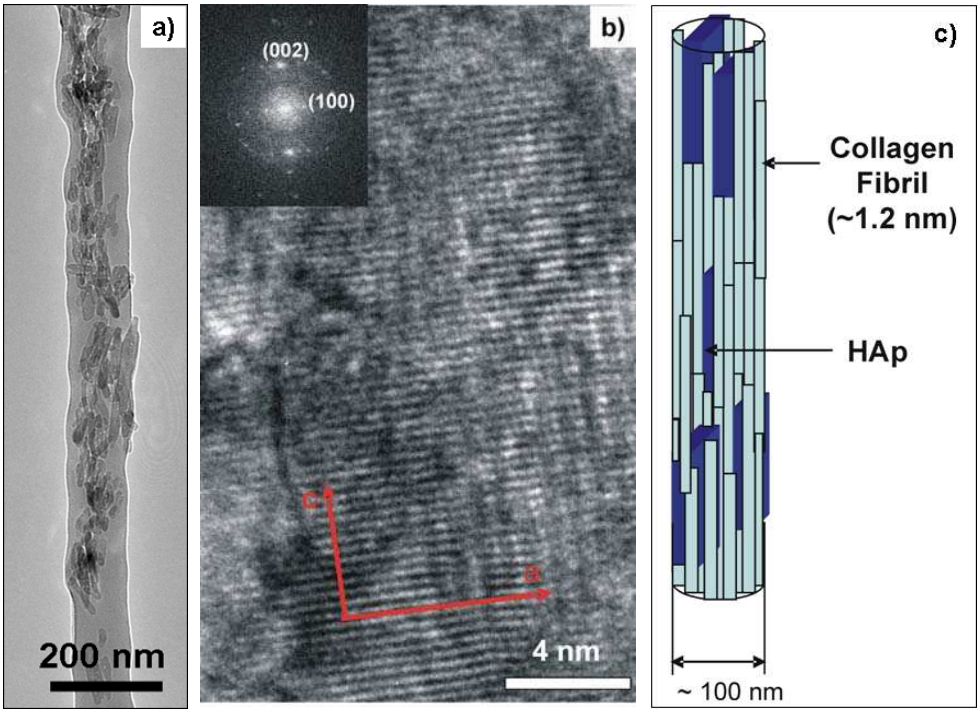

Fig. 6. a) TEM image of fiber morphology taken from a single electrospun PVA/Hap nanocomposite fiber. b) HR-TEM image and its corresponding FFT pattern (c is the fiber axis). c) schematic illustration of mineralized collagen fibrils.

3.3 Thermal analysis: DSC and TGA

In order to investigate the thermal behavior, such as melting, crystallization and formation of crystalline structure, we performed DSC measurements. Since DSC is sensitive to the thermal history of the samples, the first heating run of DSC at a rate of 10K/ min was taken into account to characterize thermal properties of all samples in the present work. The results from DSC and the characteristics observed for all systems are presented in Figure 7 and summarized in Table II.

	T_g	T_m	T_c	ΔH_m	Crystallinity %
PVA powder	41.7	218	179	65.3	47
PVA fiber	48.3	219	190	61.4	44
PVA/HAp fiber	50.3	216	187	57.8	39*

* Since the HAp nanorods do not contribute to the enthalpy of fusion for the PVA matrix, the weight only fraction of PVA is taken into consideration.

Table II. Glass transition, melting and crystallization temperatures, melting enthalpies and calculated crystallinities

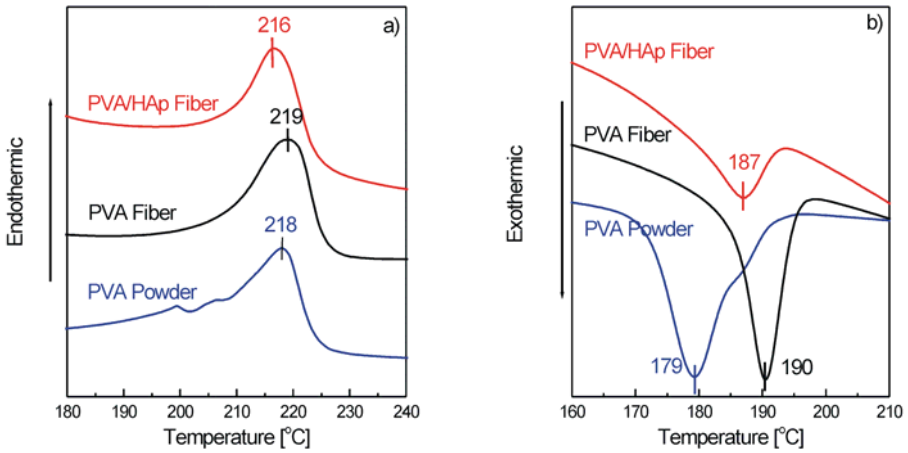

Fig. 7. DSC thermograms for the PVA powder, electrospun PVA fibers with and without HAp nanorods: a) endothermic and b) exothermic traces.

The endothermic peaks during the heating stage, which are centered at 216 -218 °C, are shown in Figure 7a. This is attributed to the melting of the crystalline PVA phase.
While the melting temperature in the electrospun fibers of pure PVA is almost unchanged compared with that in the pure PVA powder, after adding the HAp nanorods the melting temperature of the electrospun PVA/HAp NC shifts slightly to a lower value compared with others. In contrast, the melting enthalpy - the degree of crystallinity - decreases by the electrospinning, and this decrement is even more pronounced by the incorporation of HAp nanorods. A decrease in the enthalpy of fusion and the melting temperature suggests that the crystallinity and perfection of the crystal structure are reduced by HAp loading.
The lower crystallinity after electrospinning can be readily explained by the fact that the jet being ejected from a capillary under the strong electrostatic potential is highly experienced by an extensive elongational flow to stretch the polymer chains in the electrostatic filed direction and simultaneously evaporation of the solvent is followed within a very short time scale that generally leads to a lowering of the temperature (like quenching). Due to such an extremely high elongational flow rate as well as the very limited time scale during the electrospinning, the polymer chains are forced to align parallel to the fiber direction. As a consequence, the molecules in the electrospun fibers exhibit a less favorable packing.

A further decrease in crystallinity after adding HAp nanorods onto the electrospun fibers indicates that there are interactions between PVA and HAp nanoparticles, i.e., the hydrogen bonding between them. The intense hydrogen bonding can also change the chain configuration around the interfacial region of HAp nanorods, induced most likely by the amorphous layer around them. In other words, the well dispersed HAp nanorods within the electrospun fibers readily generate defects in the crystalline phase of PVA. As a consequence, less heat is needed to destroy the hydrogen bonding or to set the PVA chains free to melt, thus resulting in a decreasing melting temperature.

To determine the crystallization temperature (T_c), the samples were heated up to 250°C, kept at this temperature for 5 min and then cooled down at a rate of 10°C/min. Figure 7b shows the exotherms upon cooling from the melt. The crystallization temperature significantly increases upon electrospinning (ΔT_c= +11°C, comparing the PVA powder with the electrospun fibers of PVA) and then decreases with incorporation of the HAp nanorods (ΔT_c= -3 °C compared with the electrospun fibers of PVA/HAp NC to those of the electrospun PVA fibers). However, it should be noted that T_c for the electrospun fibers with and without HAp is still significantly higher than that of the PVA powder. All these changes can be attributed to the formation of nuclei at an earlier stage and at a higher temperature during the cooling process. The shifting to higher temperatures upon electrospinning corresponds to a promoted rapid crystallization. This is the intrinsic nature of very rapid structure formation in the electrospinning process, and thus insufficient time is provided to form perfect crystallites in the PVA matrix than in the bulk.

The decrease in T_c in the electrospun fibers by addition of HAp nanorods may be attributed to the facts that due to higher thermal conductivity of HAp nanorods compared to that of PVA, the heat will be more diversely distributed in the samples containing the HAp nanorods. Thus, HAp nanorods provide a high degree of supercooling during the electrospinning, which leads to a rapid formation of heterogeneous crystallization nuclei. On the other hand, the hydroxyl groups presented on the surface of HAp nanorods preferentially serve as heterogeneous nucleation sites for PVA crystallization, however, due to the strong interaction between HAp nanorods and PVA molecules via hydrogen bonding the crystallization process is further confined in its dimensional reduction of the PVA molecules, thereby the crystallization process will be shortened [51]. Upon introduction of HAp into ES-fibers the T_c shifts towards a higher temperature. However, a decrement of the crystallization enthalpy is observed, which is most likely attributed to the decrease of conformation entropy due to the preferential orientation of the polymer chains.

PVA exhibits an other endotherm at 41.7 °C corresponding to the glass transition temperature (T_g) of PVA [data not shown here] [52]. The overall glass transition temperatures of the PVA matrix of the electrospun fibers with and without HAp were found to have higher temperatures compared to the PVA powder, as shown in Table 2. These results indicate that the oriented PVA chains are highly confined in the electrospun fibers and upon adding HAp to the electrospun fibers more constraints are imposed on the polymer chains due to the strong interactions (such as hydrogen bonding) between them, thereby the segmental motions of the polymer chains are greatly constricted.

Figure 8 shows typical TGA thermograms with the corresponding first order derivatives (DTGA) of weight loss as a function of temperature for ES-fibers with and without HAP along with pure PVA powder. The samples were measured in the temperature range from 30 °C up to 1000 °C with a constant rate of 10 °C/ min under nitrogen atmosphere. The TGA

and DTGA show that all samples exhibited three distinct weight loss stages at 30 - 210 °C (5 wt.-% loss of weakly physisorbed water), 210 – 400 °C (decomposition of side chain of PVA) and 400 – 540 °C (decomposition of main chain of PVA) [53]. Nevertheless, major weight losses are observed about 75 wt.-% in the range of 210-540 °C for all samples, which are corresponding to the structural decomposition of PVA.

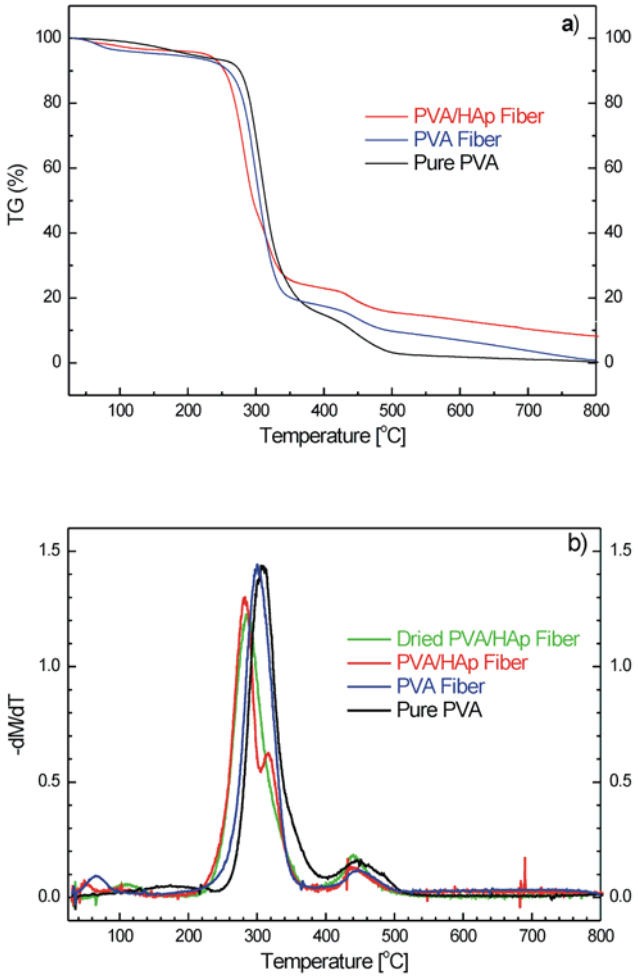

Fig. 8. a) TGA curves for the PVA powder, electrospun PVA fibers with and without HAp nanorods and b) the first order derivatives of TGA (the dried PVA/HAp nanocomposite fibers are included for comparison, as green curve).

Figure 8b shows the first order derivatives of TGA curves, revealing the temperatures at which the maximum decreases of mass occur. The temperature at the maximum mass loss rate is 308 °C for the PVA powder, 286 °C for the electrospun fibers of PVA, and 281 °C for

the electrospun fibers of PVA/HAp NC. DTGA data clearly show that the side chains of PVA are readily decomposed prior to the main chains. It can be also recognized that the thermal decomposition behavior of the electrospun PVA fibers is similar to that of the pure PVA powder. However, this process is accompanied with a decrease from 308 to 286 °C in its maximum mass loss rate upon electrospinning.

The maximum mass loss rate of the electrospun fibers of PVA/HAp NC further shifts to a lower temperature compared with that of the electrospun pure PVA. It is interesting to note here that the first derivative of the electrospun fibers of PVA/HAp NC exhibits a distinctive peak at 317 °C, which is not appearing in the TGA curve. To identify this peak we dried the electrospun PVA/HAp NC fibers in air at 80 °C for 8h, then cooled in a desiccator and TGA was carried out again. This peak completely disappears in the DTGA curve of the dried electrospun PVA/HAp NC fibers. This result clearly indicates that the peak at 312 °C arises from the loss of lattice water which may be called "structural" water or water trapped within HAp nanorods, consisting with data of Rootare and Craig [54] for the chemisorbed water layer. Over about 600 °C, all TGA diagrams become flat and mainly the inorganic residue (i.e. HAp nanorods) remains. From the amounts of the residue at 800 °C, the inorganic contents of the electrospun PHA/HAp NC are estimated of about 7.5 wt.-%.

Evidently, the thermal decomposition of both electrospun fibers of PVA and PVA/HAp NC shifts slightly toward the lower temperature range compared with bulk PVA powder. This implies that the electrospinning suppresses the thermal stability of PVA and the addition of HAp to the PVA fibers even enhances this effect.

3.4 Fourier transform infrared spectroscopy

FTIR spectroscopy was carried out to analyze any complex structural changes upon electrospinning as well as interactions between HAp and PVA. The results are summarized in Table III. The representative FTIR absorption spectrum of the HAp nanorods in the 4000 cm^{-1} to 500 cm^{-1} range is shown in Figure 9 [55]. The phosphate ions, PO_4^{3-}, are the principal

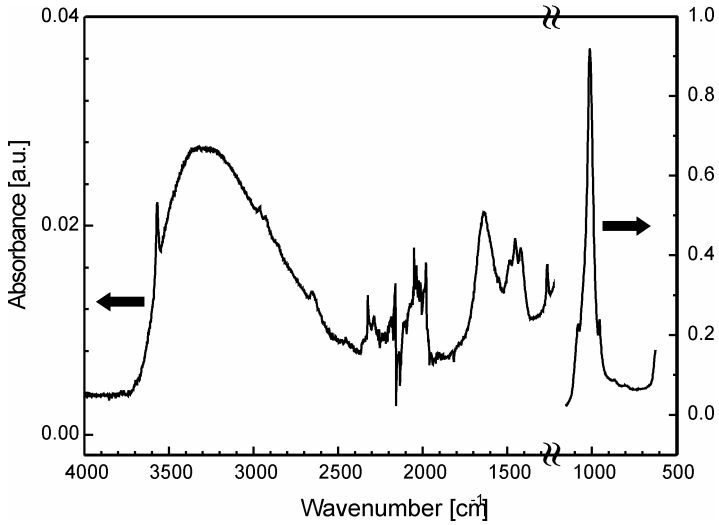

Fig. 9. FTIR spectrum of pure HAp nanorods.

HAp	PVA	PVA fiber	PVA/HAp fiber	Assignment
3567				stretching of OH
~3315				Water
	3278	3278	3296	stretching of OH
	2935	shoulder	2939	asymmetric stretching of CH_2
	2906	2914	2911	symmetric stretching of CH_2
	1710	1711	1717	stretching of CO
	1654	1657	1674	O=H, C=C
1638				Water
1485				
1453				
1421			1421	CO_2^{-3}
	1417	1418	1418	O-H, C-H bending, $\gamma(CH_2)$, δ(OH)
	1376	1374	1378	CH_2 wagging
	1325	1326	1326	δ(O-H) with CH wagging
	1238	1241	1240	C-O-C
	1143	shoulder	shoulder	Stretching of CC (crystalline sequence of PVA)
	1088	1087		stretching of CC and bending of OH (amorphous sequence of PVA)
1088			1092	symmetric stretching of PO_4^{3-}
1019			1033	asymmetric stretching of PO_4^{3-}
962			962	symmetric stretching of PO_4^{3-}
	919	917	920	Bending of CH_2
	839	831	838	Rocking of CH_2
			756	
			632	bending of OH
			599	PO_4^{3-} deformation vibration

Table III. Assignments of FTIR absorption bands of pure HAp nanorods, pure PVA powder, the electrospun fibers of PVA and PVA/HAp NC.

molecular components of HAp giving to the IR absorbance in the 550-1200 cm^{-1} region. The characteristic peaks at 962, 1019 and 1088 cm^{-1} correspond to the stretching vibration of PO_3^{-4} and at 599 cm^{-1} to the deformation vibrations of PO_3^{-4}. As other major components, OH^- ions are identified by observation of the broad band from about 3700 to 2500 cm^{-1}. The peak of this band is centered at about 3297 cm^{-1}, which is a typical assignment of the stretching mode of OH^- ions. In addition, the two distinct bands are observed at 3576 and 1639 cm^{-1}, which arise from the stretching mode and bending mode of H_2O molecules, respectively. Furthermore, some other impurity ions are also identified by the peaks

appearing in the 1490 to 1410 cm^{-1} range. These are attributed to the stretching mode of a trace amount of CO_3^{2-} groups presented in HAp.

Typical FTIR spectra of the pure PVA powder and the electrospun fibers of PVA and PVA/HAp NC along with pure HAp nanorods are shown in Figure 10. As shown in Figure 10 (curve a), the characteristic absorption bands of PVA occur at 3278 cm^{-1} (stretching of OH), 2935 cm^{-1} (asymmetric stretching of CH_2), 2906 cm^{-1} (symmetric stretching of CH_2), 1417 cm^{-1} (wagging of CH_2 and bending of OH), 1143 cm^{-1} (stretching of CO from crystalline sequence of PVA), 1088 (stretching of CO and bending of OH from amorphous sequence of PVA), 919 cm^{-1} (bending of CH_2) and 838 cm^{-1} (rocking of CH) [56].

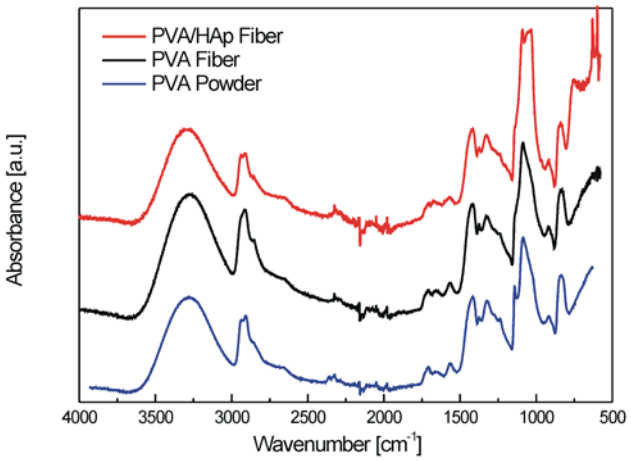

Fig. 10. FTIR spectra for the PVA powder, electrospun PVA fibers and PVA/HAp nanocomposite fibers.

The electrospun fibers of PVA show spectral features similar to that for the PVA powder, but with some extent of changes in their relative intensity and peak position (curve b in Figure 10). While the OH stretching of electrospun PVA appearing at 3278 cm^{-1} is unaltered in its position when compared to the pure PVA powder, absorption bands position changes for other peaks are observed in the electrospun PVA fibers. Minor changes occur in the carbonyl stretching in the 2900 to 2950 cm^{-1} region and a major shift appears in the CC stretching band at 1143 cm^{-1}. The asymmetric stretching band of CH_2 at 2935 cm^{-1} becomes a shoulder and its symmetric stretching band shifts to a higher value at 2914 cm^{-1} from 2906 cm^{-1}. This suggests that the electrospinning has a strong influence on the wavelength and consequently the absorption maxima of stretching vibration shifts toward higher frequencies in comparison with the pure PVA. It is important to emphasize here that the intensity of the 1143cm^{-1} band, which is associated with the CC stretching mode of PVA, is crystalline sensitive and thus is generally used for qualitative and/or quantitative analysis of PVA crystallinity [57]. Accordingly, it can be clearly recognized that the intensity of the 1143cm^{-1} band in the electrospun PVA fibers compared with pure PVA powder appears significantly changed in form of a shoulder. This result indicates that the degree of crystallinity of PVA decreases upon electrospinning, consisting with the trends observed from DSC measurements.

The FTIR spectrum of the electrospun PVA/HAp NC fibers (curve c in Figure 10) exhibits the characteristic absorption bands of PAV along with additional bands corresponding to the phosphate groups of HAp. After incorporating HAp nanorods into the PVA fibers the predominant broad absorption band associated with the OH stretching of PVA centered at 3278 cm^{-1} shifts to a higher wave number region (ν_{OH} = 3296 cm^{-1}). This result suggests that the hydrogen bonding becomes stronger in the electrospun PVA/HAp NC than in pure PVA as well as in the electrospun PVA fibers due to the increase in the number of OH groups by adding of HAp.
In addition, the major absorption band of PO_4^{3-} stretching appearing at 1019 cm^{-1} in the HAp spectrum, moves to 1033 cm^{-1}. This red shift might be attributed to the interactions between PVA molecules and HAp particles. Also the spectra of PVA adsorbed on HAp influence clearly the recovering of the carbonyl stretching region (see in the red circled area). Furthermore, the overall PVA crystallinity decreases by loading of HAp within the electrospun fibers, which is clearly evidenced by weakening of the crystalline band at 1143 cm^{-1}.
It is of interest to note here that the absorption bands associated with H_2O molecules distinctly appear at 3576 cm^{-1} and 1639 cm^{-1} in the spectrum of HAp. The higher peak at 3576 cm^{-1} is completely missing in the electrospun fibers of PVA/HAp NC, while the peak at 1639 cm^{-1} still exists in the spectrum despite of a large extent of reduction in its intensity. In conjunction with the TGA results we confirmed that the former band at 3576 cm^{-1} is identified with the loosely physisorbed water at the surface of HAp nanorods, whereas the latter arises from the chemisorbed molecular water within the HAp lattice.

4. Conclusions

In the present work we demonstrate a powerful technique for fabricating biocompatible and biodegradable PVA/HAp nanocomposite fibers in order to mimic mineralized hard tissues for bone regeneration purpose by applying the electro spinning process. Various techniques, including TEM, HR-TEM, SEM, XRD, DSC, TGA, FTIR spectroscopy were performed to characterize the resulting electrospun PVA/HAp composite nanofibers in comparison with pure PVA and PVA/HAp nanocomposites before electrospinning. Morphological investigation showed that the HAp nanoparticles exhibit nanoporous morphology, which provides enlarged interfaces being a prerequisite for physiological and biological responses and remodeling to integrate with the surrounding native tissue. The most striking physiochemical feature of the electrospun PVA/HAp composite nanofibers is that the HAp nanorods are preferentially oriented parallel to the longitudinal direction of the electrospun PVA fibers as confirmed by electron microscopy and XRD. This feature bears strong resemblance to the nanostructure of mineralized hard tissues serving as building block of bone. Furthermore, the PVA as matrix and HAp nanorods as inorganic phases strongly interact through hydrogen bonds within the electrospun PVA/HAp nanocomposite fibers. The strong bonding due to the presence of a great extent of OH groups in the PVA polymer and the HAp nanorods leads improved thermal properties. The hybrid electrospinning shown in the present work provides great potential as a convenient and straightforward technique for the fabrication of biomimicked mineralized hard tissues suitable for bone and dentin replacement and regeneration. However, a great challenge still exists mainly in how to stabilize the electrospun PVA/Hap nanofibers when in contact with an aqueous medium. Such deficiency could be resolved by proper chemical and/or physical treatments of the material that are currently under investigation.

5. Experimental procedure

5.1 Materials and electrospinning process

All experiments utilized commercial grade PVA (Aldrich) with an average molecular weight, M_w, of about 115.000, and a degree of hydrolysis of 98-99%. The HAp nanoparticles were of commercial grade Ostim® from *aap* Implantate AG, Germany. At first, an aqueous solution of 7 wt.-% pure PVA was prepared by dissolving the PVA polymer in distilled water at 80 °C with vigorous stirring for about 8h. To obtain electrospinnable solution, the prepared 7 wt.-% aqueous solution of PVA was slowly cooled to room temperature, sonicated for 30 min and kept at this temperature for one night, to eliminate air bubbles. In addition, to prepare the solution of PVA/HAp nanocomposite the 7.5 wt.-% HAp was added into the 7 wt.-% aqueous solution of PVA. This solution was also vigorously stirred with a magnetic stir for at least 8h at room temperature, followed by sonication for 2h to ensure homogeneity. Electrospinning was carried out at room temperature in a vertical spinning configuration, using a 1 mm inner diameter flat-end needle with a 5 cm working distance. The applied voltages were in the range from 3 kV to 20 kV, driven by a high voltage power supply (Knürr-Heizinger PNC, Germany). The electrospun fibers were collected either directly on Cu-grids or glide glasses.

5.2 Characterization

5.2.1 Electron microscopy

The morphology and particle size of the as-received HAp were investigated by conventional transmission electron microscopy (TEM) (JEOL 200CX operated at 200 kV) as well as by high-resolution TEM (Philips CM200 FEG\ST Lorentz electron microscope with a field emission gun and at an acceleration voltage of 200 kV). Micrographs were recorded with a 1k*k, 14 bit CCD-camera (model multiscan, Gatan company, USA) and fed to a computer for on-line image processing (Digital Micrograph 3.3.1, Gatan company, USA). Samples for electron microscopy were prepared by dropping aqueous solution of HAp and direct electrospinning of PVA/HAp NC on Cu-grids covered with an ultra thin carbon layer for characterization of HAp particles and their spatial dispersion within the electrospun fibers, respectively. The size and morphology of the electrospun fibers were investigated by field emission gun environmental scanning electron microscopy (FEG-ESEM, Philips ESEM XL 30 FEG). The diameter of the fibers and their size distribution were analyzed by measuring over 200 fibers in the randomly recorded FEG-ESEM micrographs, using image analysis software (Analysis, Soft Imaging System Co., Germany). Samples for FEG-ESEM were directly electrospun on the slide glasses and followed by Au sputtering.

5.2.2 Wide-Angle X-Ray Diffraction (WAXD)

To analyze the crystalline structure of the PVA powder, the electrospun (ES) PVA fiber and the ES-PVA/HAp NC fibers wide-angle X-ray scattering (WAXS) was performed with a Seifert XRD 3000 using CuKα radiation (λ = 1.54056 Å). The tube source was operated at 40 kV and 30 mA. Scans were run over a 2θ range of 10-60° with a step of 0.05° and a dwell time of 1 s.

5.2.3 Differential scanning calorimetry (DSC) and Thermogravimetric analysis (TGA)

DSC measurements were conducted to measure the glass-transition temperatures (T_g), the melting and crystallization behavior with a Mettler-Toledo DSC 820 under a nitrogen atmosphere. The samples were sealed in aluminum pans and were heated and cooled in the

temperature range 25 to 250 °C in the DSC instrument with a rate of 10 °C/min. The weight of each sample was approximately 0.5 mg. The DSC temperature and heat flow values were calibrated with indium as standard. The degree of relative crystallinity X_c, was estimated from the endothermic area by the following equation (1):

$$X_c = \Delta H_f \, / \, \Delta H_f^o \tag{1}$$

where ΔH_f is the measured enthalpy of fusion from DSC thermograms and ΔH_f^o is the enthalpy of fusion for 100% crystalline PVA (ΔH_m = 138.6 J/g from literature) [43].
Thermo gravimetric analysis (TGA) was performed using a Perkin-Elmer TGA7 by heating from room temperature to 750°C at a heating rate of 20°C/min under a nitrogen flow.

5.2.4 Fourier Transform Infrared spectroscopy (FTIR)

An FTIR spectrometer (FTIR-Spectrometer S2000, Perkin-Elmer) equipped with a fixed 100 μm diameter aperture and a mercury-cadmium-telluride (MCT) detector was used to analyze the absorbance in the wave number range of 500-4000 cm^{-1} with a resolution of 2 cm^{-1}.

6. References

[1] Weiner S, Traub W. Bone structure: from angstroms to microns. FASEB 1992;6:879–85.
[2] Rho JY. Kuhn-Spearing L, Zioupos P. Mechanical properties and the hierarchical structure of bone. Med. Eng. Phys.1998; 20: 92-102.
[3] Fratzl P. Characterizing natural fibre composites with hierarchical structure. Fibre Diffraction Rev 2002;210:32-9
[4] Park JB, Lakes RS. Biomaterials, 2nd ed. New York: Plenum Publishing Co, 1992. p. 194.
[5] Ravaglioli A, Krajewski A, Bioceramics: Materials, Properties, Applications. Chapman and Hall, London, UK, 1992.
[6] Elliott JC. Structure and Chemistry of the Apatites and Other Calcium Orthophosphated; Elsevier; Amsterdam, 1994.
[7] Butler, W.T. & Ritchie, H. The nature and functional significance of dentin extracellular matrix proteins. Int. J. Dev. Biol. 39, 169–179 (1995).
[8] Park J, Lutz R, Felszeghy E, Wiltfang J, Nkenke E, Neukam FW, Schlegel KA. The effect on bone regeneration of a liposomal vector to deliver BMP-2 gene to bone grafts in peri-implant bone defects. Biomaterials 2007; 28: 2772-82.
[9] A. Kocialkowski, W.A. Wallace and H.G. Prince, Clinical experience with a new artificial bone graft: preliminary results of a prospective study. Injury 21 (1990), pp. 142–144.
[10] Dujardin E, Mann S. Bio-inspired materials chemistry. Adv Mater 2002; 14: 775-88
[11] Kikuchi M, Itoh S, Ichinose S, Shinomiya K, Tanaka J. Self-organization mechanism in a bone-like hydroxyapatite/collagen nanocomposite synthesized in vitro and its biological reaction in vivo. Biomaterials 2001; 22: 1705-11.
[12] Yamaguchi I, Tokuchi K, Fukuzaki H, Koyama Y, Takakuda K, Monma H, Tanaka J. Preparation and mechanical properties of chitosan/hydroxyapate nanocomposites. Bioceramics 2000;192-1:673-76.
[13] Chen F. Wang ZC, Lin CJ. Preparation and characterization of nano-sized hydroxyapate particles and hydroxyapatite/chitosan nanocomposite for use in biomedical materials, Mater. Lett. 2002; 57: 658-62.
[14] Liao SS, Cui FZ, Zhang W, Feng QL. Hierarchically Biomimetic Bone Scaffold Materials: Nano-HA/Collagen/PLA Composite. J. Biomed. Mater. Res. Part B: Appl. Biomater. 2004; 69B: 158-65.

[15] Deng XM, Hao JY, Wang CS. Preparation and mechanical properties of nanocomposites of poly(D,L.lactide) with Ca-defient hydroxyapatite nanocrystals. Biomaterials 2002; 22: 2867-73.
[16] Wei J, Li YB, Chen WQ, Zuo Y. A study on nanocomposite of hydroxyapatite and polyamide. J Mater Sci 2003;38:3303-06.
[17] Hung M, Feng JQ, Wang JX, Zhang XD, Li YB, Yan YG. Synthesis and characterization of nano-HA/PA66 composites. J Mater Sci: Mater Med 2003;14:655-60.
[18] Hartegerink JD, Beniash E, Stupp SI. Self-Assembly and Mineralization of Peptide-Amphiphilie Nanofibers. Science 2001;294:1684-88.
[19] Marouf H A, Quayle A A, Sloan P. In vitro and in vivo studies with collagen/hydroxyapatite implants. Int J Oral Maxillofac Implants 1990;5:148–54.
[20] C. Du, F.Z. Cui, X.D. Zhu and K. de Groot, Three-dimensional nano-HAp/collagen matrix loading with osteogenic cells in organ culture. J Biomed Mater Res 1999;44:407–15.
[21] Reneker, D. H.; Chun, I. Nanometre diameter fibres of polymer, produced by electrospinning. Nanotechnology 1996;7:216-23.
[22] Kim GM, Wutzler A, Radusch HJ, Michler GH, Simon P, Sperling RA, Parak WJ. One-Dimensional Arrangement of Gold Nanoparticles by Electrospinning. Chem. Mater. 2005;17:4949-57.
[23] Dror Y, Salalha W, Khalfin RL, Cohen Y, Yarin AL, Zussman E. Carbon Nanotubes Embedded in Oriented Polymer Nanofibers by Electrospinning. Langmuir 2003;19:7012-20.
[24] Kim GM, Michler GH, Pötschke P. Deformation processes of ultrahigh porous multiwalled carbon nanotubes/polycarbonate composite fibers prepared by electrospinning. Polymer 2005;46:7346-51
[25] Fong H, Liu W, Wang CS, Vaia RA. Generation of electrospun fibers of nylon 6 and nylon 6-montmorillonite nanocomposite. Polymer 2002;43:775-80.
[26] Kim GM, Lach R, Michler GH, Chang CH. The Micromechanical Deformation Process of Electrospun Polymer Nanocomposite Fibers. Macromol. Rapid Commun. 2005;26:728-33.
[27] Kim Michler GH, Ania F, Balta Calleja FJ. Temperature-dependence of polymorphism in electrospun nanofibres of PA6 and PA6/clay nanocomposite, Polymer 2007;48:4814-23.
[28] Kim GM, Lach R, Michler GH, Pötschke P, Albrecht K. Relationships between phase morphology and deformation mechanisms in polymer nanocomposite nanofibres prepared by electrospinning process. Nanotechnology 2006;17:963-72.
[29] Wang M, Singh H, HattonTA, Rutledge GC. Field-responsive superparamagnetic composite nanofibers by electrospinning. Polymer 2004;45:5505-14.
[30] de Bruijn JD, van Blitterswijk CA, Davies JE. Initial bone matrix formation at the hydroxyapatite interface in vitro. J Biomed Mater Res 1995;29:89–99.
[31] Hamadouche M, Sedel L. Ceramics in orthopaedics. J Bone Joint Surg Br 2000;82:1095–1099.
[32] Traub W, Arad T, Weiner S. Three-dimensional ordered distribution of crystals in turkey tendon collagen fibers. Proc. Natl. Acad. Sci. USA. 1989;86:9822-26.
[33] Hench LL. Bioceramics: From Concept to Clinic. J. Am. Ceram. Soc. 1991, 74, 1487-510.
[34] W. Suchanek, M. Yoshimura, Processing and Properties of Hydroxyapatite-Based Biomaterials For Use as Hard Tissue Replacement Implants. J. Mater. Res. 1998, 13, 94-117.
[35] Hench LL. Bioceramics. J. Am. Ceram. Soc. 1998;81:1705-28.
[36] LeGeros RZ. Calcium phosphates in oral biology and medicine. Monogr Oral Sci 1991;15:1-21.

[37] Kobayashi H, PVA-HAp nanocomposites for artificial cornea. Adv in Sci & Tech 2006;53:9-16.
[38] Scotchford CA, Cascone MG, Downes S, Giusti P, Osteoblast responses to collagen-PVA bioartificial polymers in vitro: the effects of cross-linking method and collagen content. Biomaterials 1998;19:1–11.
[39] Aoi K, Takasu A, Okada M. DNA-based polymer hybrids. Part I. Compatibility and physical properties of poly(vinyl alcohol)/DNA sodium salt blend. Polymer 2000;41:2847–53.
[40] Tamada Y, Ikada Y. In: E. Chiellini, P. Giusti, C. Migliaresi and L. Nicolais, Editors, Polymers in medicine 2, Plenum Publishing Company, New York (1986), p. 101.
[41] Stejskal, J.; Kratochvil, P.; Helmstedt, M. Polyaniline Dispersions. 5. Poly(vinyl alcohol) and Poly(N-vinylpyrrolidone) as Steric Stabilizers. Langmuir 1996;12:3389-92.
[42] Finch, C. A. Poly(vinyl alcohol) Development; Wiley: Chichester, England, 1992; pp 18-32.
[43] Peppas NA, Merrill EW, Differential scanning calorimetry of crystallized PVA hydrogels. J. Appl. Polym. Sci. 1976;20:1457-65.
[44] Rusu VM, Ng CH, Wilke M, Tiersch B, Fratzl P, Peter MG, Size-controlled hydroxyapatite nanoparticles as self-organized organic-inorganic composite materials, Biomaterials 2005;26:5414-26.
[45] Sato K, Kogure T, Iwai H, Tanaka J, Atomic-Scale {10-10} Interfacial Structure in Hydroxyapatite Determined by High-Resolution Transmission Electron Microscopy, J Am Ceram Soc 2002; 85:3054–58.
[46] Sutter B, Ming DW, Clearfield A, Hossner LP. Mineralogical and Chemical Characterization of Iro-, Manganese-, and Copper-Containing Synthetic Hydroxyapatites. Soil Sci Soc Am J 2003;67:1935-1942.
[47] Astala R, Stott MJ. First Principles Investigation of Mineral Component of Bone:CO_3 Substitution in Hydroxyapate. Chem. Mater. 2005;17:4125-33.
[48] Klug HP, Alexander LE. X-ray diffraction precedures for polycrystallite and amorphous materials. New York: Wiley; 1974.
[49] Ricciardi, R.; Auriemma F, Rosa CD, Laupretre F. X-ray Diffraction Analysis of Poly(vinyl alcohol) Hydrogels, Obtained by Freezing and Thawing Techniques. Macromolecules 2004;37;1921-27.
[50] Bunn CW, Crystal structure of polyvinyl alcohol. Nature 1948, 161, 929-30.
[51] Pritchard, J. G. Poly(vinyl alcohol)--Basic Properties and Uses, Polymer Monographs; Gordon and Breach Science: New York, 1970; Vol 4.
[52] Strawhecker KE, Manias E. Structure and Properties of Poly(vinyl alcohol)/Na+ Montmorillonite Nanocomposites. Chem Mater 2000;12:2943-49.
[53] Gimenez, V.; Mantecom, A.; Cadiz, V. Modification of poly(vinyl alcohol) with acid chlorides and crosslinking with difunctional hardeners. J Polym Sci Part A:Polym Chem 1996;34:925-34.
[54] Rootare HM, Craig RG. Vapor phase adsorption of water on hydroxyapatite, J Dental Res 1977;56:1437-48.
[55] Rey C, Shimizu M, Collins B, Glimcher MJ, Resolution-enhanced Fourier transform infrared spectroscopy study of the environment of phosphate ion in the early deposits of a solid phase calcium phosphate in bone and enamel and their evolution with age: 2. Investigations in the v_3 PO_4 domain, Calcif. Tissue Int., 1990, 46,384.
[56] Ding B, Kimura E, Sato T, Fujita S, Shiratori S, Fabrication of blend biodegradible nanofibrous nonwoven mats via multi-jet electrospinning, Polymer 2004;45:1895-1902.
[57] Tadokoro H, Seki S, Nitta I. Some information on the infrared absorption spectrum of polyvinyl alcohol from deuteration and pleochroism. J. Polym. Sci. 1956;22:563-66.

Nanofibers

Edited by Ashok Kumar

ISBN 978-953-7619-86-2
Hard cover, 438 pages
Publisher InTech
Published online 01, February, 2010
Published in print edition February, 2010

“There’s Plenty of Room at the Bottom” this was the title of the lecture Prof. Richard Feynman delivered at California Institute of Technology on December 29, 1959 at the American Physical Society meeting. He considered the possibility to manipulate matter on an atomic scale. Indeed, the design and controllable synthesis of nanomaterials have attracted much attention because of their distinctive geometries and novel physical and chemical properties. For the last two decades nano-scaled materials in the form of nanofibers, nanoparticles, nanotubes, nanoclays, nanorods, nanodisks, nanoribbons, nanowhiskers etc. have been investigated with increased interest due to their enormous advantages, such as large surface area and active surface sites. Among all nanostructures, nanofibers have attracted tremendous interest in nanotechnology and biomedical engineering owing to the ease of controllable production processes, low pore size and superior mechanical properties for a range of applications in diverse areas such as catalysis, sensors, medicine, pharmacy, drug delivery, tissue engineering, filtration, textile, adhesive, aerospace, capacitors, transistors, battery separators, energy storage, fuel cells, information technology, photonic structures and flat panel displays, just to mention a few. Nanofibers are continuous filaments of generally less than about 1000 nm diameters. Nanofibers of a variety of cellulose and non-cellulose based materials can be produced by a variety of techniques such as phase separation, self assembly, drawing, melt fibrillation, template synthesis, electro-spinning, and solution spinning. They reduce the handling problems mostly associated with the nanoparticles. Nanoparticles can agglomerate and form clusters, whereas nanofibers form a mesh that stays intact even after regeneration. The present book is a result of contributions of experts from international scientific community working in different areas and types of nanofibers. The book thoroughly covers latest topics on different varieties of nanofibers. It provides an up-to-date insightful coverage to the synthesis, characterization, functional properties and potential device applications of nanofibers in specialized areas. We hope that this book will prove to be timely and thought provoking and will serve as a valuable reference for researchers working in different areas of nanofibers. Special thanks goes to the authors for their valuable contributions.

How to reference

In order to correctly reference this scholarly work, feel free to copy and paste the following:

Gyeong-Man Kim (2010). Fabrication of Bio-Nanocomposite Nanofibers Mimicking the Mineralized Hard Tissues via Electrospinning Process, Nanofibers, Ashok Kumar (Ed.), ISBN: 978-953-7619-86-2, InTech, Available from: http://www.intechopen.com/books/nanofibers/fabrication-of-bio-nanocomposite-nanofibers-mimicking-the-mineralized-hard-tissues-via-electrospinni

INTECH
open science | open minds

InTech Europe
University Campus STeP Ri
Slavka Krautzeka 83/A
51000 Rijeka, Croatia
Phone: +385 (51) 770 447
Fax: +385 (51) 686 166
www.intechopen.com

InTech China
Unit 405, Office Block, Hotel Equatorial Shanghai
No.65, Yan An Road (West), Shanghai, 200040, China
中国上海市延安西路65号上海国际贵都大饭店办公楼405单元
Phone: +86-21-62489820
Fax: +86-21-62489821